

A STUDY OF ^3He CAPTURE IN LIGHT NUCLEI

C. E. WALTHAM[†], S. H. CHEW^{††}, J. LOWE and J. M. NELSON

Department of Physics, University of Birmingham, Birmingham B15 2TT, England

and

A. R. BARNETT

Department of Physics, University of Manchester, Manchester M13 9PL, England

Received 10 November 1980

(Revised 27 September 1982)

Abstract: Excitation functions at $\theta = 90^\circ$ have been measured for $^{16}\text{O}(^3\text{He}, \gamma_{0-2,3-5,6})^{19}\text{Ne}$, $^{15}\text{N}(^3\text{He}, \gamma_{0,1-4})^{18}\text{F}$, $^{14}\text{N}(^3\text{He}, \gamma_{0,1,2,3})^{17}\text{F}$, and $^{20}\text{Ne}(^3\text{He}, \gamma_{0+1})^{23}\text{Mg}$, in the range $E_{^3\text{He}} = 3\text{--}19$ MeV. The first reaction has also been studied at $\theta = 40^\circ$. Excitation functions at 90° have also been measured for $^{40}\text{Ca}(^3\text{He}, \gamma_{0-2})^{43}\text{Ti}$ for $E_{^3\text{He}} = 4\text{--}17$ MeV and $^4\text{He}(^3\text{He}, \gamma_{0+1})^7\text{Be}$ for $E_{^3\text{He}} = 19\text{--}26$ MeV. Angular distributions have been measured for the first four reactions.

For the most excitation functions, a broad peak is observed, several MeV wide, centred at about $E_x \approx 20$ MeV. Superimposed on this, in some cases, are narrower peaks, with width ≈ 1 MeV. Energies and widths have been extracted for all resonances.

Cluster-model calculations have been carried out, using methods similar to those which have proved successful for low-lying states in $A = 18\text{--}19$ nuclei. No satisfactory correspondence with the present results was found. The shell model has been used to calculate $\Gamma_{^3\text{He}}$ and Γ_γ for $1\hbar\omega$ excitations in the final nuclei. These generally show good agreement with the trends of the experimental data. The results are consistent with the excitation of the giant dipole resonance in ^3He capture, but much more weakly than in proton capture.

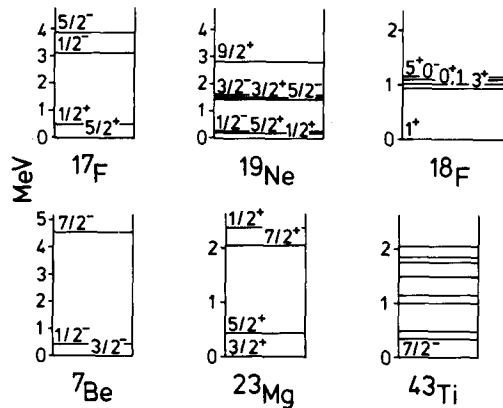
E NUCLEAR REACTIONS ^{16}O , ^{15}N , ^{14}N , ^{20}Ne , ^{40}Ca , $^4\text{He}(^3\text{He}, \gamma)$, $E = 3\text{--}19$ MeV; measured $\sigma(E, \theta)$. ^{19}Ne , $^{18,17}\text{F}$, ^{23}Mg , ^{43}Ti deduced levels, J , π , Γ , $\Gamma(^3\text{He})$, Γ_γ . Enriched target.

1. Introduction

The present paper reports a study of ^3He capture in light nuclei, covering the excitation region of the giant dipole resonance. Prior to the present investigation, work on ^3He capture had been carried out by several groups^{1–13}). The motivation

[†] Present address: Physics Department, University of British Columbia, Vancouver, BC, Canada V6T 2A6.

^{††} Present address: Nuclear Physics Laboratory, Keble Road, Oxford OX1 3RH, England.



Level Diagrams

Fig. 1. Level diagrams for states studied here.

for the present work was twofold. Firstly, the previous data were insufficiently extensive to establish the general characteristics of ^3He capture at these energies. For example, there was no clear picture of the extent to which the giant dipole resonance (GDR) influences ^3He capture in light nuclei. The second motivation was to search for ^3He cluster states and to study the validity of the cluster model at high excitations. Considerable success has recently been achieved by Buck and Pilt¹⁴⁻¹⁶) in the application of a realistic cluster model to nuclei just beyond ^{16}O for states at $E_x \lesssim 10$ MeV observed in transfer reactions. They predicted several more highly excited states, with energies accessible to capture reactions.

The experiments reported here consist of measurements of the excitation functions at 90° (lab) for $^4\text{He}(^3\text{He}, \gamma)^7\text{Be}$, $^{14}\text{N}(^3\text{He}, \gamma)^{17}\text{F}$, $^{15}\text{N}(^3\text{He}, \gamma)^{18}\text{F}$, $^{16}\text{O}(^3\text{He}, \gamma)^{19}\text{Ne}$, $^{20}\text{Ne}(^3\text{He}, \gamma)^{23}\text{Mg}$ and $^{40}\text{Ca}(^3\text{He}, \gamma)^{43}\text{Ti}$ over the energy range $E_{^3\text{He}} \approx 3\text{--}19$ MeV (except for $^4\text{He}(^3\text{He}, \gamma)^7\text{Be}$, for which it was $E_{^3\text{He}} = 19\text{--}26$ MeV). An excitation function at 40° (lab) was measured for $^{16}\text{O}(^3\text{He}, \gamma)^{19}\text{Ne}$ for $E_{^3\text{He}} = 5\text{--}11$ MeV. Gamma-ray angular distribution measurements were made at several energies for capture to ^{17}F , ^{18}F , ^{19}Ne and ^{23}Mg . The experiments and results are reported in sects. 2–4. Sects. 5 and 6 describe respectively the application of the cluster model and the shell model to the data. Sect. 7 summarises the results. Energy level diagrams for the final nuclei involved in these reactions are shown in fig. 1.

2. Experimental method

All measurements were carried out at the Oxford Nuclear Physics Laboratory, using ^3He beams from the EN tandem accelerator (for $E_{^3\text{He}} = 3\text{--}19$ MeV) and

from the folded tandem (for $E_{^3\text{He}} = 16\text{--}26$ MeV). Beam currents of 10–50 nA were used.

The targets used were gaseous, with the exception of ^{40}Ca . The gas cell had a nickel front window, $0.45\text{ mg}\cdot\text{cm}^{-2}$ thick, and a gold beam stop. The pressure was variable between zero and 200 Torr and the cell length was 6.1 cm. Where the cross section was very low, as in the case of $^3\text{He} + ^4\text{He}$, shielding the beam stop was not sufficient to reduce the background to an acceptable level, and so a remote beam dump was employed. Tungsten alloy shielding was used close to the most intense sources of background, in order to attenuate both neutrons and γ -rays.

Frequent monitoring of the energy calibration of the detector was required. For this purpose, the gas target was fitted with a retractable plunger with a ^{13}C target mounted at the end. When introduced into the beam, this produced copious 15.11 MeV γ -rays from the $^{13}\text{C}(^3\text{He}, \alpha\gamma)^{12}\text{C}$ reaction, which provided a convenient monitor of the detector energy calibration. Counting rates in the NaI detector were typically about $10^4/\text{sec}$ during most of the measurements. At these relatively low rates, count-rate dependent gain shifts were negligible with the phototubes used here (Space Research Corp., type 75B01), so that the slight change in counting rate when the ^{13}C was inserted in the beam was of no consequence for the gain calibration.

For the ^{40}Ca experiments, a target chamber with a remote beam dump was used. Ca targets were evaporated up to a thickness of $500\text{ }\mu\text{g}\cdot\text{cm}^{-2}$ onto Ta backings, and transferred under vacuum into the target chamber.

Capture γ -rays were detected in a 25 cm diameter \times 30 cm NaI(Tl) detector, by methods which have been described in detail elsewhere^{10,11,17}). The NaI crystal was surrounded by a cylindrical anticoincidence shield, 10 cm thick, of NE102A plastic scintillator. The shield served to veto cosmic-ray signals in the NaI detector, and also to improve the detector resolution by vetoing events in which some of the incident γ -ray energy escaped from the NaI in the form of annihilation or bremsstrahlung photons. A Pb collimator, 10 cm thick, with a tapered hole at the centre, was mounted in front of the detector allowing a 15 cm diameter circle to be illuminated on the front face of the NaI crystal. Target-to-detector distances between 18 and 42 cm were used during the experiments, the larger distances being used for angular distribution measurements or when the best energy resolution was required.

For some experiments an additional anticoincidence shield was used. This consisted of a disc of NE102A scintillator, 6.5 cm thick, placed over the front face of the NaI crystal, behind the Pb collimator. The main purpose of this was to veto events in which a 511 keV annihilation γ -ray escaped out of the front face of the NaI. This was particularly troublesome in the study of capture to ^{17}F , since the first excited state of this nucleus is at 495 keV. Thus the single-escape peak from the γ_0 line lies on top of the full-energy peak of the γ_1 line. Fig. 2 shows the response of the detector, with the front anticoincidence shield in operation, to a

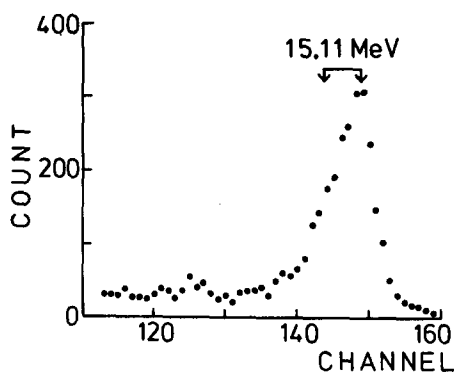


Fig. 2. Response of the NaI detector, with its anticoincidence shields, to a 15.11 MeV γ -ray. The arrows indicate the positions of the full-energy and single-escape peaks for the 15.11 MeV γ -ray.

15.11 MeV γ -ray; it can be seen that the line shape is such that contamination of the γ_1 line by the escape peak of the γ_0 line was negligible.

A block diagram of the electronics is shown in fig. 3. Signals were taken from the dynodes and anodes of the six SRC 75B01 phototubes which viewed the NaI crystal. The anode signals were passed through a high-level discriminator (HLD)

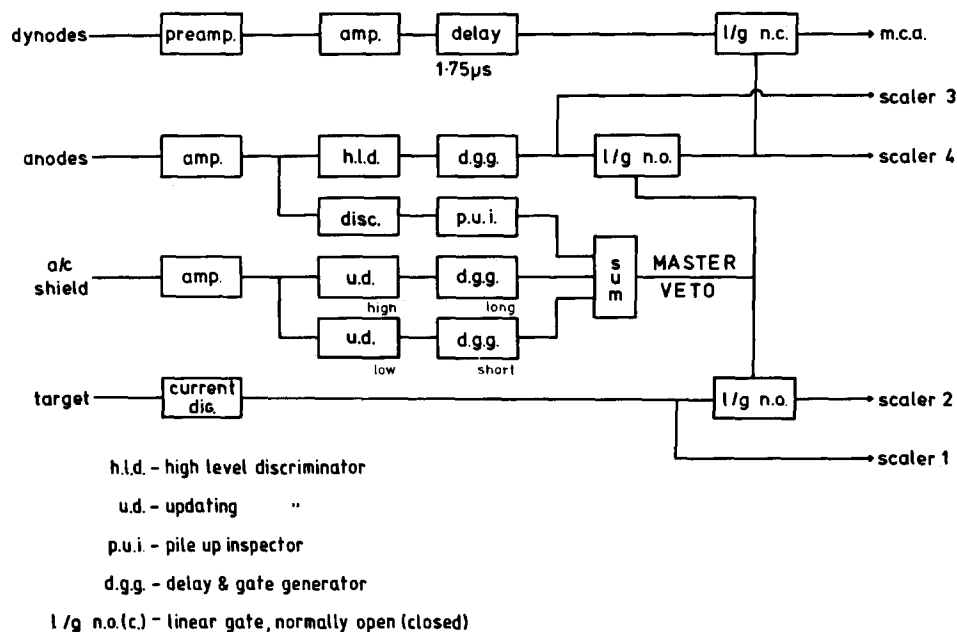


Fig. 3. Block diagram of the electronics.

and also to a pile-up inspector, which examined the signals for pairs of pulses occurring within 2 μsec of each other¹⁷).

The signals from the anticoincidence shield were split and fed to two discriminators and gate generators. The upper discriminator was set high enough so that it triggered only on cosmic rays in the shield. The corresponding gate generator then produced a pulse about 10 μsec wide, in order to veto signals in the NaI from the decays of cosmic-ray muons ($t_{\frac{1}{2}} = 2.2 \mu\text{sec}$) which stopped in the crystal. The lower discriminator was set low enough to be triggered by a 511 keV photon, and the inhibit signal was set short for prompt events.

All veto signals were combined to produce a master veto signal. Unless vetoed by this signal, pulses from the HLD opened a linear gate which passed the amplified dynode signals to a 512-channel multichannel analyser for analysis. The master veto signal was also used to inhibit the output pulse train from the current digitiser. Thus the overall counting losses due to the system dead time resulting from pile-up and cosmic-ray rejection was determined directly. The correction was always less than 10 %.

Spectra accumulated in the multichannel analyser were transferred to a PDP-10 computer for analysis.

Yield-to-background ratios were low and therefore cross sections could only be extracted using a program which fitted line shapes and backgrounds for each spectrum¹⁷). Line-shape parameters were obtained by fitting to a 15.11 MeV peak measured from the $^{13}\text{C}(^3\text{He}, \alpha\gamma)^{12}\text{C}$ reaction. This procedure was repeated for each configuration of detector used, as the line shape varied with the target thickness and the detector-to-target distance.

The energy resolution of the detector was typically 5 %. With this resolution the yields in γ -ray peaks corresponding to final states, or groups of states, separated by more than 500 keV could be extracted reasonably well. For $^{14}\text{N}(^3\text{He}, \gamma)^{17}\text{F}$, the γ_0 and γ_1 peaks are separated by 495 keV. In this case, measurements were made initially with a thick target to give an excitation function for γ_{0+1} (unresolved). Then the region of interest was re-examined using a target thin enough to enable the γ_0 and γ_1 yields to be extracted separately. For $^{16}\text{O}(^3\text{He}, \gamma)^{19}\text{Ne}$, the γ_0 and γ_{1+2} peaks are only 240 keV apart. While it is clearly not possible to separate the yields to these, we were able to establish which of the two peaks was resonating in the case of two of the three resonances observed in the γ_{0-2} excitation function.

Because of the difficulty in measuring the absolute yield using a collimated detector, absolute values of the cross sections were determined in separate measurements, made at several suitable energies, with an uncollimated detector. The detector efficiency for this case was calculated using the program DETECT¹⁸).

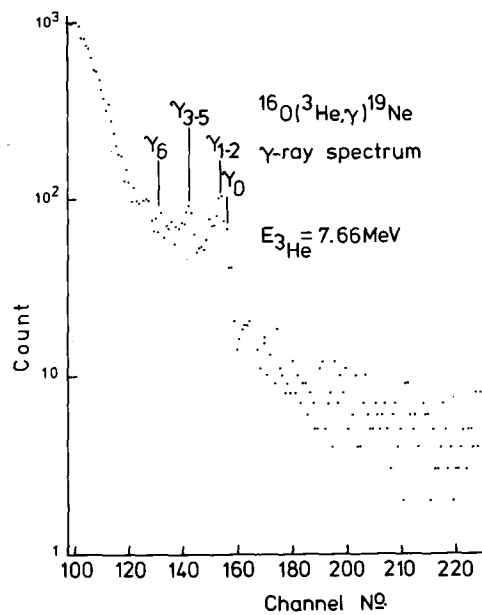


Fig. 4. Pulse-height spectrum in the NaI detector for $^{16}\text{O}(^3\text{He}, \gamma)^{19}\text{Ne}$.

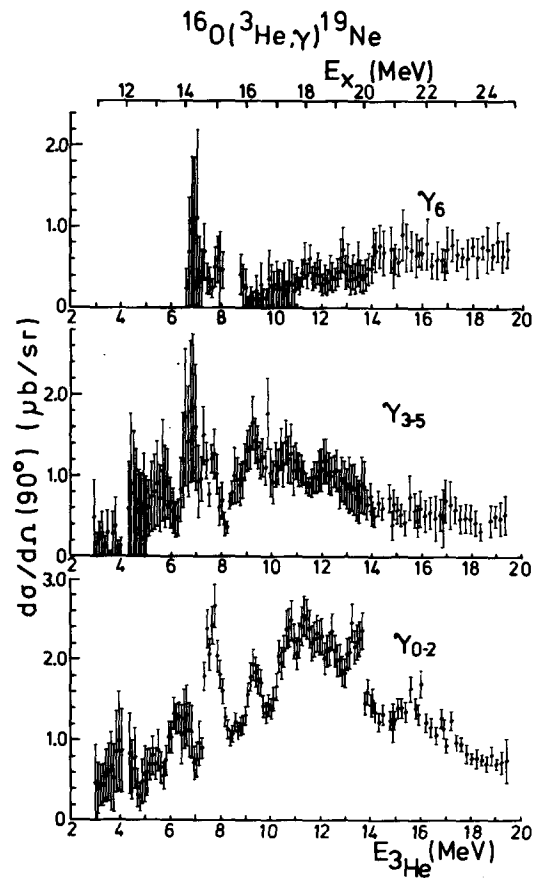


Fig. 5. $d\sigma/d\Omega$ (lab) for $^{16}\text{O}(^3\text{He}, \gamma)^{19}\text{Ne}$ at 90° .

3. Results

The results are presented in figs. 4–17. For the excitation functions, shown in figs. 5, 7, 9, 11, 14, 15 and 17, the errors shown are relative only, and arise almost entirely from uncertainties in the separation of yields for peaks from those for neighbouring peaks and for the background. There is an additional absolute error of $\pm 20\%$, in general, due to uncertainty in the detector efficiency. Angular distributions are shown in figs. 8, 10, 13 and 14.

The excitation functions, which are discussed below, show several resonances, with widths between 0.4 and 6 MeV. In some cases narrow resonances are superimposed on a broader resonance. If each resonance is interpreted as a single state,

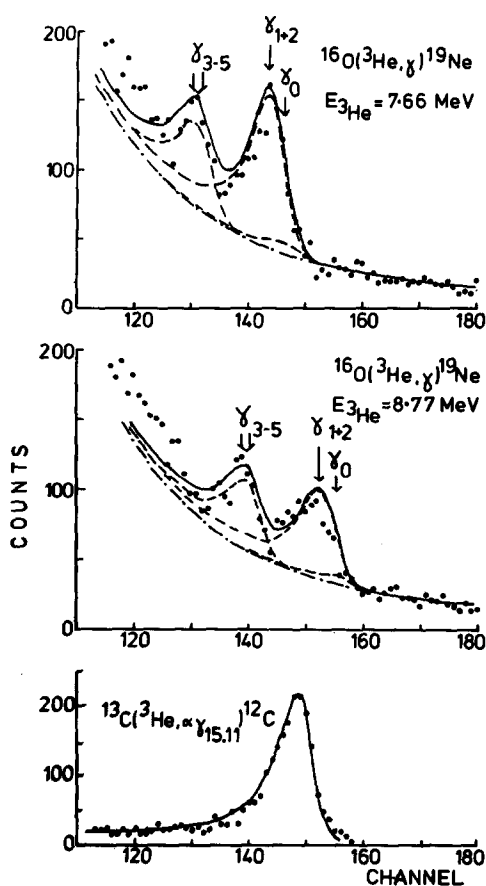


Fig. 6. Pulse-height spectra in the NaI detector from ^3He on ^{16}O on (upper graph) and off (middle graph) the resonance in γ_{0-2} at $E_{^3\text{He}} = 7.65$ MeV. The dash-dot curve shows the fitted background. Dashed curves show the result of added γ_0 , γ_{1-2} and γ_{3-5} individually to this background, and the solid curve is the overall fit. The lower graph shows the 15.11 MeV calibration line and its fitted curve.

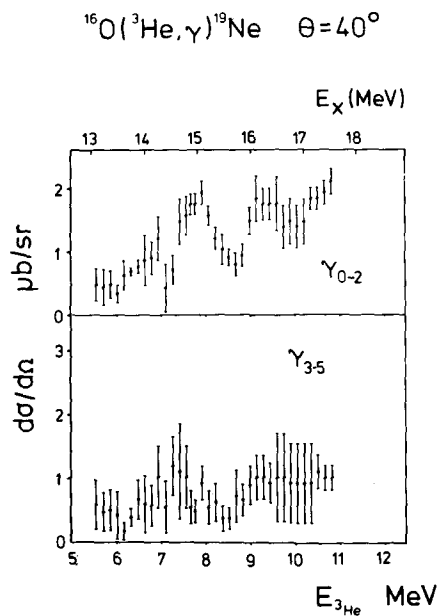


Fig. 7. $d\sigma/d\Omega$ (lab) for $^{16}\text{O}(^3\text{He}, \gamma)^{19}\text{Ne}$ at 40° .

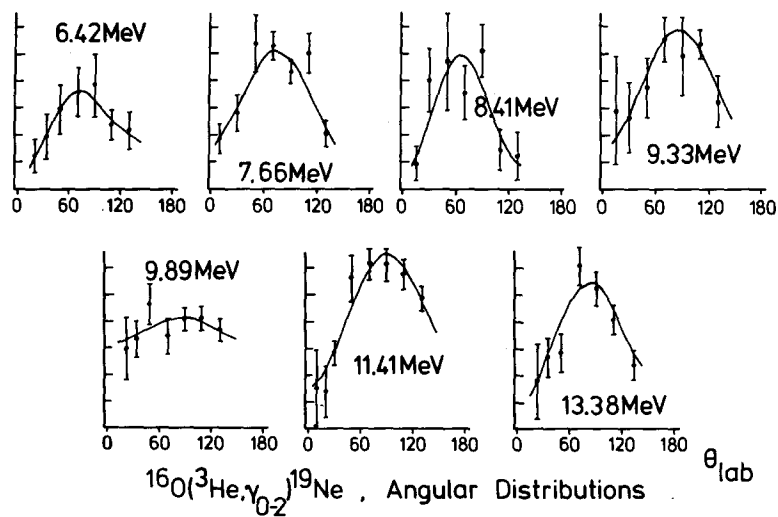
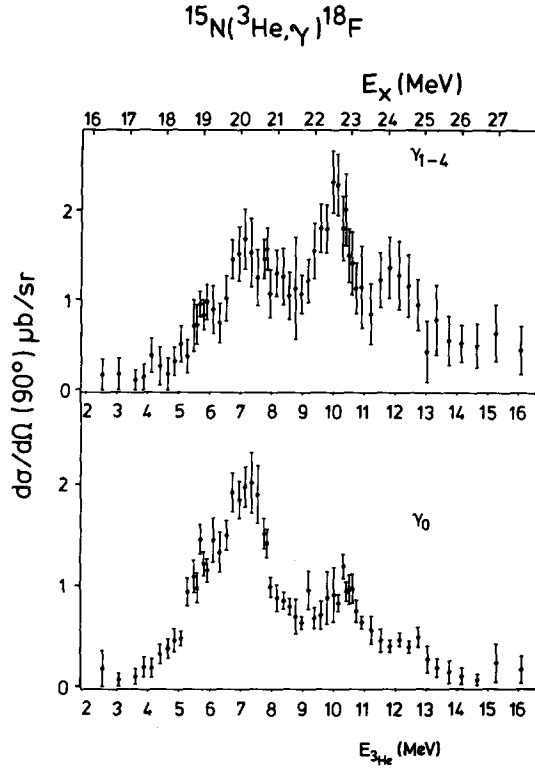


Fig. 8. Angular distributions for $^{16}\text{O}(^3\text{He}, \gamma)^{19}\text{Ne}$. The graphs are identified by the ^3He beam energy. The curves are the Legendre polynomial fits using the parameters of table 2.

Fig. 9. $d\sigma/d\Omega$ (lab) for $^{15}\text{N}(^3\text{He}, \gamma)^{18}\text{F}$.

the Breit-Wigner formula

$$\sigma = \frac{\pi}{k^2} \frac{(2J+1)}{(2J_1+1)(2J_2+1)} \frac{\Gamma_{^3\text{He}}\Gamma_\gamma}{(E-E_0)^2 + \frac{1}{4}\Gamma^2}$$

enables the quantity $(2J+1)\Gamma_{^3\text{He}}\Gamma_\gamma$ to be extracted from the measured cross section. Values derived in this way will not be accurate for the present results, since the assumption that the resonances are isolated and are incoherent with the background is not likely to be valid in general. However, in the absence of sufficient information to carry out a full multi-level analysis, the values based on the above assumptions were extracted and are given in table 1.

A Legendre polynomial fit was carried out for each angular distribution. The measured values were fitted by the expression

$$\frac{d\sigma}{d\Omega} = A_0 \left(1 + \sum_{k=1}^{k_{\max}} a_k P_k(\cos \theta) \right).$$

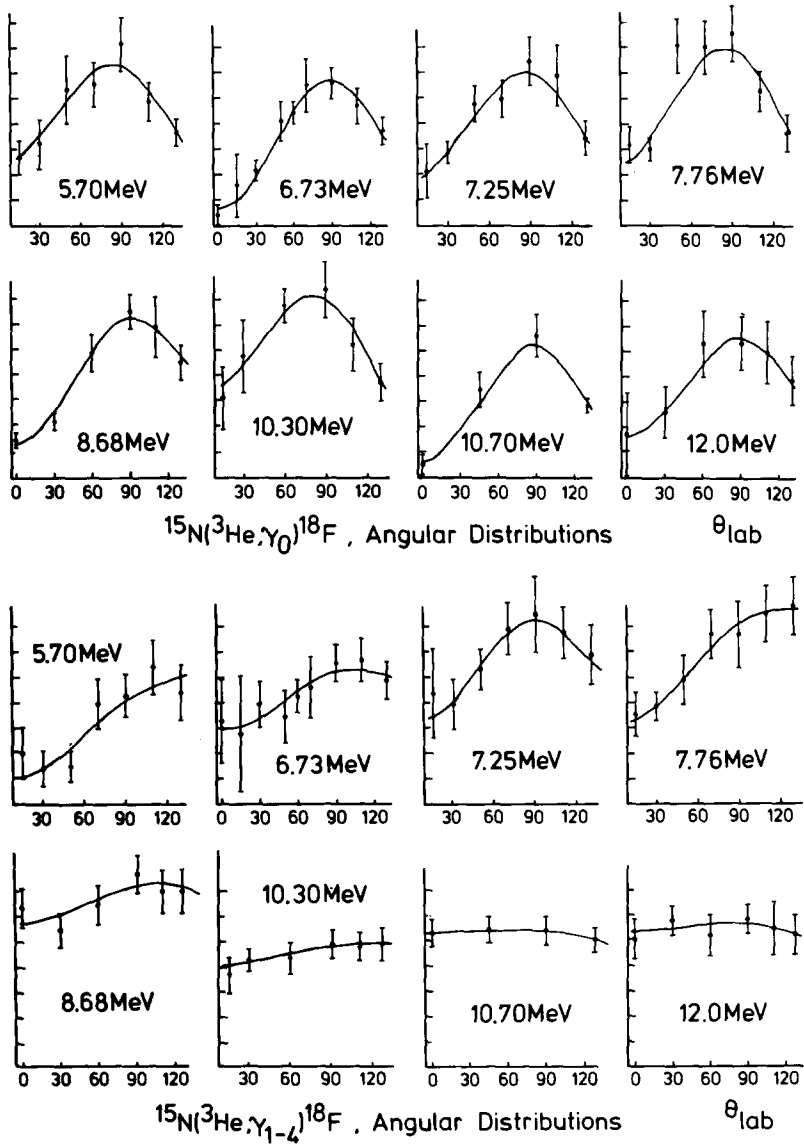


Fig. 10. Angular distributions for $^{15}\text{N}(^3\text{He}, \gamma)^{18}\text{F}$. The graphs are identified by the ^3He beam energy. The curves are the Legendre polynomial fits using the parameters of table 2.

A satisfactory fit was found for a value of k_{max} of 2 in most cases, or 3 for some of the ^{19}Ne data. The values of a_k are listed in table 2, and the values of A_0 were used to determine σ from $d\sigma/d\Omega$ (90°) for use in the Breit-Wigner formula.

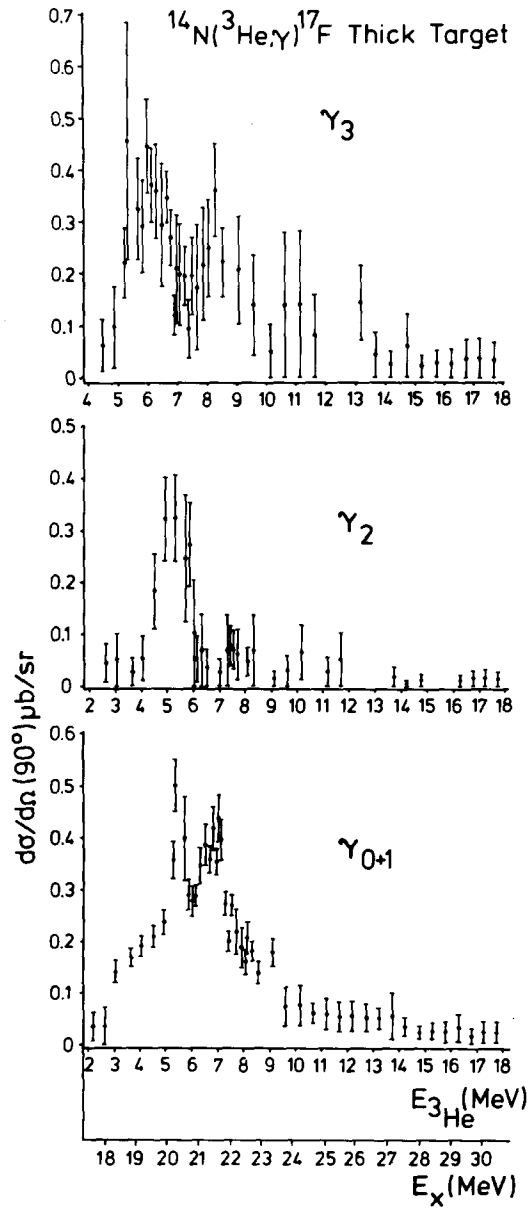


Fig. 11. $d\sigma/d\Omega$ (lab) for $^{14}\text{N}(^3\text{He}, \gamma)^{17}\text{F}$ (thick target).

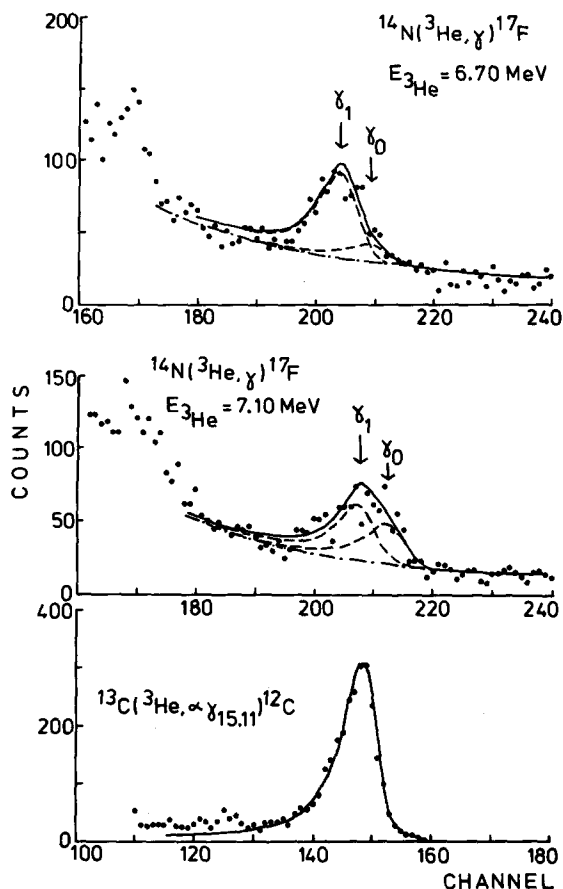


Fig. 12. Pulse-height spectra in the NaI detector from ^3He on ^{15}N , both on (upper curve) and off (lower curve) the resonance at $E_{^3\text{He}} = 6.70$ MeV. The curves are identified in the caption to fig. 6.

3.1. THE REACTION $^{16}\text{O}(^3\text{He}, \gamma)^{19}\text{Ne}$ ($Q = 8.44$ MeV)†

Fig. 4 shows a typical gamma-ray spectrum for this reaction, and fig. 5 gives the 90° excitation functions for γ_{0-2} , γ_{3-5} and γ_6 . Resonances are seen at $E_x = 13.8$, 14.88 and 16.24 MeV ($E_{^3\text{He}} = 6.37$, 7.65 and 9.26 MeV) in γ_{0-2} . Extracted widths are given in table 1. There is a broad, underlying structure in γ_{0-2} , a peak centred at $E_x \approx 18$ MeV with a width of about 4.4 MeV. This appears somewhat more weakly in γ_{3-5} . No structure is seen in γ_0 .

As mentioned above, the yields to the γ_0 and γ_{1+2} groups are separated by only

† Ref. 19).

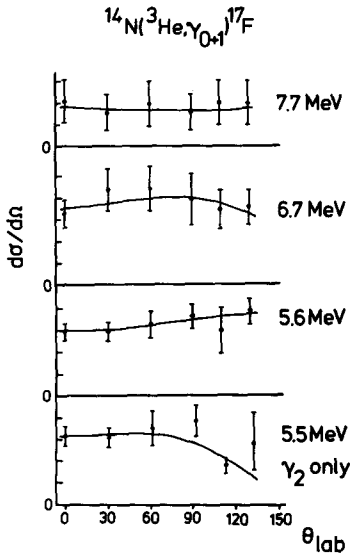


Fig. 13. Angular distributions for $^{14}\text{N}(^3\text{He}, \gamma_{0+1})^{17}\text{F}$ at beam energies of 5.6, 6.7 and 7.7 MeV, and for $^{14}\text{N}(^3\text{He}, \gamma_2)^{17}\text{F}$ at a beam energy of 5.5 MeV, together with Legendre polynomial fits.

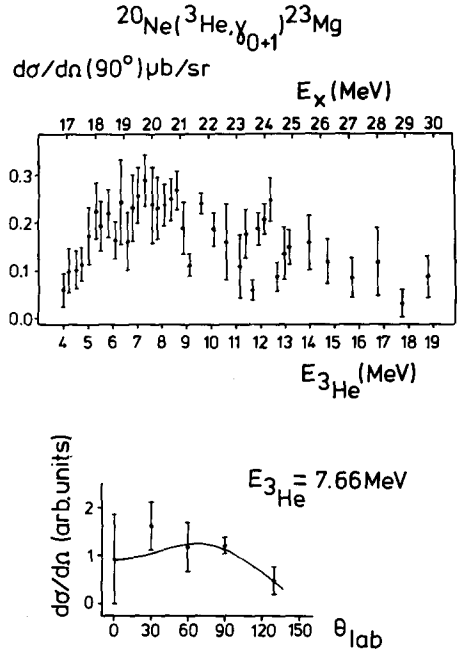


Fig. 14. $d\sigma/d\Omega$ (lab) and angular distributions for $^{20}\text{Ne}(^3\text{He}, \gamma)^{23}\text{Mg}$.

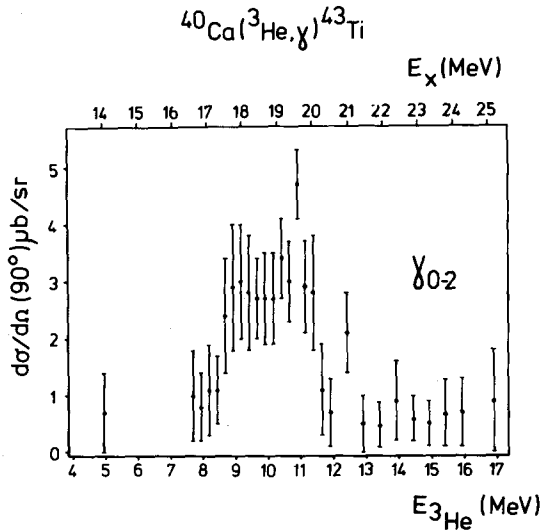


Fig. 15. $d\sigma/d\Omega$ (lab) for $^{40}\text{Ca}(^3\text{He}, \gamma)^{43}\text{Ti}$.

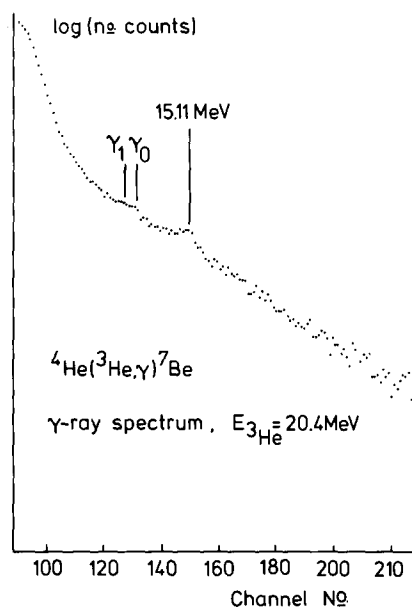


Fig. 16. Pulse-height spectrum in the NaI detector from ^3He and ^4He at a beam energy of 20.4 MeV.

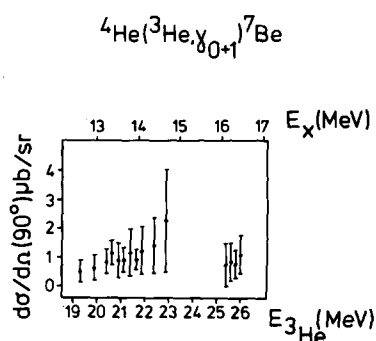


Fig. 17. $d\sigma/d\Omega$ (lab) for $^4\text{He}(^3\text{He},\gamma)^7\text{Be}$.

TABLE I
Resonances observed in ^3He capture reactions

Final nucleus	E_x (MeV)	$\Gamma_{c.m.}$ (MeV)	Decay mode	$(2J+1)\Gamma_{^3\text{He}}\Gamma_\gamma$ (keV ²)
<i>fine structure</i>				
^{17}F	20.4 ± 0.1	0.7 ± 0.1	γ_1	33 ± 13
	21.3 ± 0.1	0.9 ± 0.1	γ_1	74 ± 23
	20.1 ± 0.2	1.07 ± 0.16	γ_2	63 ± 29
^{18}F	19.00 ± 0.15	0.5 ± 0.15	γ_{1-4}	29 ± 20
	20.1 ± 0.2	1.6 ± 0.1	γ_0	1230 ± 300
			γ_{1-4}	1110 ± 280
	22.7 ± 0.2	1.2 ± 0.1	γ_0	580 ± 190
			γ_{1-4}	1560 ± 440
^{19}Ne	24.1 ± 0.2	1.4 ± 0.3	γ_{1-4}	1410 ± 710
	13.8 ± 0.25	0.67 ± 0.25	γ_{1+2}	30 ± 17
	14.88 ± 0.13	0.62 ± 0.13	γ_{1+2}	89 ± 44
	16.24 ± 0.13	0.40 ± 0.13	γ_{1+2}	18 ± 4
<i>broad structure</i>				
^{19}Ne	18.4 ± 0.5	4.4 ± 0.5	γ_{0-2}	17000 ± 5300
^{23}Mg	19.5 ± 1.0	5.5 ± 1.0	γ_{0+1}	2500 ± 1500
^{43}Ti	18.7 ± 0.2	3.1 ± 0.3	γ_{0-2}	12300 ± 4400

TABLE 2
Legendre coefficients for ^3He capture

Final nucleus	$E_{^3\text{He}}$	Decay channel	a_1	a_2	a_3
^{17}F	5.55	γ_{0+1}	-0.01 ± 0.14	-0.19 ± 0.08	
	6.70		0.13 ± 0.17	-0.19 ± 0.17	
	7.70		-0.03	0.03 ± 0.24	
	5.50	γ_2	0.63 ± 0.18	-0.34 ± 0.18	
^{18}F	5.70	γ_0	0.19 ± 0.13	-0.69 ± 0.17	
	6.73		0.01 ± 0.12	-0.86 ± 0.14	
	7.25		0.12 ± 0.14	-0.74 ± 0.19	
	7.76		0.19 ± 0.10	-0.79 ± 0.05	
	8.68		-0.12 ± 0.13	-0.60 ± 0.14	
	10.30		0.28 ± 0.14	-0.69 ± 0.21	
	10.70		0.05 ± 0.11	-0.91 ± 0.14	
	12.00		0.01 ± 0.23	-0.64 ± 0.30	
	5.70	γ_{1-4}	-0.60 ± 0.20	-0.18 ± 0.27	
	6.73		-0.18 ± 0.13	-0.22 ± 0.18	
	7.25		-0.02	-0.46 ± 0.17	
	7.76		-0.35 ± 0.14	-0.19 ± 0.17	
	8.68		-0.10 ± 0.11	-0.10 ± 0.12	
	10.30		-0.12 ± 0.11	-0.06 ± 0.14	
	10.70		0.02 ± 0.10	-0.05 ± 0.12	
	12.00		0.02 ± 0.13	-0.07 ± 0.14	
^{19}Ne	6.42	γ_{0-2}	0.05 ± 0.27	-0.48 ± 0.45	-0.42 ± 0.38
	7.66		0.35 ± 0.17	-0.70 ± 0.28	-0.17 ± 0.25
	8.41		0.52 ± 0.40	-0.54 ± 0.59	-0.79 ± 0.43
	9.33		0.08 ± 0.19	-0.74 ± 0.31	
	9.89	γ_{3-5}	-0.01 ± 0.10	-0.18 ± 0.15	
	11.41		0.01 ± 0.09	-0.64 ± 0.13	
	13.38		0.18 ± 0.15	-0.83 ± 0.22	-0.04 ± 0.24
^{23}Mg	7.66	γ_{0+1}	0.51 ± 0.26	-0.48 ± 0.26	

250 keV and are not resolved. Fig. 6 shows the spectra observed on and off the resonance at $E_{^3\text{He}} = 7.65$ MeV, together with fits to these spectra using the known line shape. A 15.11 MeV calibration spectrum is also shown. While the relative yields, especially for the weaker line (γ_0), cannot be extracted reliably, there are indications that it is the γ_1 transition that is resonating in the peaks at $E_{^3\text{He}} = 7.65$ and 9.26 MeV. The decay mode of the resonance at $E_{^3\text{He}} = 6.33$ MeV has not been established.

Fig. 7 shows the 40° excitation function for γ_{0-2} and γ_{3-5} for the range

$E_{^3\text{He}} = 5\text{--}11$ MeV. A comparison of this with the 90° excitation function shows no new peaks; each resonance seen in γ_{0-2} at 90° appears again at 40° . Very little structure is seen in γ_{3-5} . The absolute accuracy of the 40° excitation functions is $\pm 25\%$.

The angular distributions measured are shown in fig. 8. A Legendre polynomial analysis is shown in table 2.

3.2. THE REACTION $^{15}\text{N}(^3\text{He}, \gamma)^{18}\text{F}$ ($Q = 14.16$ MeV)[†]

Fig. 9 shows the 90° excitation functions for γ_0 and γ_{1-4} . Resonances can be seen at $E_x = 20.1$ and 22.7 MeV ($E_{^3\text{He}} = 7.1$ and 10.2 MeV) in γ_0 and γ_{1-4} and at $E_x = 24.1$ MeV ($E_{^3\text{He}} = 11.9$ MeV) in γ_{1-4} . Again the overall structure is several MeV wide and is centred at around 20 MeV excitation energy.

The results of the angular distribution measurements are shown in fig. 10.

3.3. THE REACTION $^{14}\text{N}(^3\text{He}, \gamma)^{17}\text{F}$ ($Q = 15.84$ MeV)^{††}

Fig. 11 shows the 90° excitation functions for γ_{0+1} , γ_2 and γ_3 , over the $E_{^3\text{He}} = 2\text{--}18$ MeV region. The target was thick, i.e. equivalent to an energy spread of about 500 keV, and thus it was not possible to separate γ_0 and γ_1 whose energy difference is less than this. Peaks are seen at $E_x = 20.5$ and 21.3 MeV ($E_{^3\text{He}} = 5.7, 6.6$ MeV) in γ_{0+1} and these may lie on top of some broader structure, centred at about $E_x = 20$ MeV. A single, isolated peak at $E_x = 20.1$ MeV ($E_{^3\text{He}} = 5.2$ MeV) is seen in γ_2 . No clear structure is seen in γ_3 , although a broad feature similar to that seen in γ_0 may be present.

These measurements were repeated with a thinner target, with an energy spread of 200 keV. Only the region of higher yield, $E_{^3\text{He}} = 3\text{--}11$ MeV, was covered. As with ^{19}Ne , the separation of yields to closely spaced final states is difficult, but the spectra shown in fig. 12 indicate that the two resonances appearing in γ_{0+1} result from the γ_1 channel only.

Fig. 13 shows the measured angular distributions for the two narrow peaks in γ_1 and one at an energy above these. The angular distribution at the γ_2 peak is also shown. The beam energy loss in the target was about 300 keV during these measurements.

3.4. THE REACTION $^{20}\text{Ne}(^3\text{He}, \gamma)^{23}\text{Mg}$ ($Q = 13.36$ MeV)[‡]

The 90° excitation function for γ_{0+1} is shown in fig. 14. No attempt was made to separate γ_0 and γ_1 . A broad peak is seen, centred at $E_x \approx 20$ MeV, with a width of

[†] Ref. ¹⁹).

^{††} Ref. ²⁰).

[‡] Ref. ²¹).

about 5.5 MeV. No narrow resonances are seen, although there may be structure at $E_{^3\text{He}} = 12\text{--}13$ MeV. Fig. 14 also shows the angular distribution taken at the point of maximum yield.

3.5. THE REACTION $^{40}\text{Ca}(^3\text{He}, \gamma)^{43}\text{Ti}$ ($Q = 9.41$ MeV)[†]

Fig. 15 shows the 90° excitation function for γ_{0-2} . A broad peak is seen, centred at $E_x \approx 19$ MeV, with a width of about 3 MeV. The gap in the data from $E_{^3\text{He}} = 5\text{--}7.5$ MeV was due to a large peak at $E_\gamma = 15.11$ MeV from the $^{13}\text{C}(^3\text{He}, \alpha\gamma)^{12}\text{C}$ reaction on carbon contamination which obscured the capture γ -rays for beam energies in this range.

3.6. THE REACTION $^4\text{He}(^3\text{He}, \gamma)^7\text{Be}$ ($Q = 1.59$ MeV)^{††}

Great difficulty was experienced in extracting yields from the measured γ -ray spectra (fig. 16). The low Q -value and the loss of energy to recoil resulted in the capture γ -ray peaks lying in the region of high background. Fig. 17 shows the excitation function. Most of the measurements are upper limits on the yield. The gap in the data at $E_{^3\text{He}} = 23\text{--}25$ MeV is again due to the obscuring of the capture γ -ray peak by a high yield of 15.11 MeV γ -rays.

3.7. THE ANGULAR DISTRIBUTIONS

In general, the angular distributions for each reaction follow the same pattern in that they are peaked forward of 90° . Thus Legendre polynomial fitting gives negative a_2 values and usually small positive a_1 coefficients. For ^{19}Ne a negative a_3 coefficient was needed in four distributions. These results are consistent with a predominantly dipole character for all transitions observed, but with a significant component of opposite parity needed to move the peak forward of 90° .

4. Comparison with other work

The only direct comparison between the present results and those of other workers is in the case of $^{14}\text{N}(^3\text{He}, \gamma)^{17}\text{F}$, which has also been studied by Mo *et al.*¹²⁾. These authors measured the γ_{0+1} (unresolved) yield over the range $E_{^3\text{He}} = 3.5\text{--}7$ MeV. They observed three resonances, at $E_{^3\text{He}} = 4.35, 5.36$ and 6.28 MeV ($E_x = 19.42, 20.25$ and 21.01 MeV). Two of these are in moderate agreement with the results of the present work ($E_x = 20.4$ and 21.3 MeV, see table 1),

[†] Ref. ²¹).

^{††} Ref. ²²).

although the agreement of the general shape of the excitation function is not good. Mo *et al.* assigned spins to these resonances on the assumption that they all decay to the ground state. The present results show that this is not the case.

Work on the mirror reaction, $^{14}\text{N}(t, \gamma)^{17}\text{O}$, by Linck *et al.*²³⁾ has shown very similar cross sections to those found in the present work. The γ_0 yield is somewhat more structured than for ^3He capture, and two clear peaks were seen at 20.39 ($\frac{5}{2}^{\pm}$ or $\frac{7}{2}^-$) and 20.15 MeV ($\frac{3}{2}^{\pm}$). Only one broader peak was observed at 20.2 ± 0.3 MeV in the ^3He capture. Because of the high Q -value of 18.62 MeV for $^{14}\text{N}(t, \gamma)^{17}\text{O}$, the triton energy was lower than the ^3He energy for the corresponding excitation energy. Hence Γ_t was much smaller and analogous states too broad to be resolved in ^3He capture were observed clearly in triton capture.

Greater similarity exists between the γ_1 yields. Peaks were seen by Linck *et al.* at 19.76 ($\frac{3}{2}^{\mp}$), 20.58 ($\frac{1}{2}^{\pm}$) and 21.05 MeV ($\frac{3}{2}^{\mp}$). The first does not appear clearly in $(^3\text{He}, \gamma)$, possibly for the same reasons as outlined above, but the other two correspond well to the ^{17}F states at 20.4 and 21.3 MeV. The strengths are somewhat smaller for triton capture, probably because $\Gamma_t < \Gamma_{^3\text{He}}$ for these states.

The work of Del Bianco *et al.*⁶⁾ on $^{12}\text{C}(^3\text{He}, \gamma)^{15}\text{O}$, although not directly comparable with our work, covers a similar energy range to ours and is close to the mass region we have studied in most detail. The qualitative features of their results follow the same general pattern as that found here for $A = 17-19$; there is a broad maximum in the yield over a region of about 7 MeV, with some structure superimposed on it. Del Bianco *et al.* analyse this excitation function into five Breit-Wigner resonances each with width < 1 MeV, although their results could also be interpreted to have a broad underlying structure, as discussed for some of the present results in sect. 6.

5. Analysis – the cluster model

The cluster-model work of Buck and Pilt¹⁴⁻¹⁶⁾, referred to above, consists of an attempt to apply the model to calculate ^3He and ^4He cluster states in nuclei at the bottom of the sd-shell. Initially the cluster-core potential was derived¹⁴⁾ from the folding model, and this was fitted by a simple analytic form, known as the “cosh” potential:

$$V(r) = -V_0 \frac{1 + \cosh(R/a)}{\cosh(r/a) + \cosh(R/a)},$$

where R and a are respectively the radius and diffuseness of the potential. Parameters for this well were derived by fitting the energies of cluster states calculated in the potential to the experimental energies of states found to be strongly excited in tri-nucleon transfer reactions. Many such states were found to

be well fitted by a single potential well of cosh form, together with a spin-orbit term. The model was first applied in this form to ^{19}F .

The model predicts higher states than those observed in 3-nucleon transfer. In particular, the parameters that fit the low-lying states predict a group of states the analogues of which in ^{19}Ne fall in the region of excitation studied here. At least one of these states may have a large ^3He capture strength. The most likely candidate is the state for which $2N + L$ (the number of oscillator quanta in the ^3He cluster) = 9, $L = 1$ and $J^\pi = \frac{3}{2}^-$. This can decay to the $J^\pi = \frac{5}{2}^+$ first excited state. In fact, the state is predicted at $E_x \approx 15$ MeV, with a radiative width of $^{(16)} \Gamma_\gamma = 18.4$ eV. It therefore seemed a strong candidate for identification with the resonance found here at $E_x = 14.88$ MeV. An experimental lower limit on the radiative width of this resonance can be derived from the value of $(2J + 1)\Gamma_{^3\text{He}}\Gamma_\gamma = (89 \pm 40)$ keV² (table 1), since $\Gamma_{^3\text{He}}$ cannot be greater than the total width, $\Gamma = 0.62$ MeV. At this limit, $\Gamma_\gamma = (36 \pm 18)$ eV, in good agreement with the cluster-model prediction.

Before a valid comparison can be made, however, it was necessary to extend Buck and Pilt's calculation in order to treat unbound states correctly. In ref. ¹⁴⁾, these were defined in an approximate way by imposing a boundary condition ($V = \infty$) at $r = 12$ fm. Thus the calculated energies are not accurate, and, more important, the particle decay widths of the resulting states cannot readily be calculated.

The ^3He cluster states in ^{19}F and ^{19}Ne were therefore recalculated using a cosh potential for the ^3He - ^{16}O interaction, and defining unbound states by the points at which the phase shift of the scattered wave, δ_L , increases through $\frac{1}{2}\pi$. Their widths were then given by

$$\Gamma_{\text{cluster}} = 2 \left(\frac{dE}{d\delta_L} \right)_{E=E_0}.$$

Resonances were found in ^{19}F and ^{19}Ne and these are shown in fig. 18. The well used differed slightly from that of Buck and Pilt: the depth was 110.2 MeV instead of 116, and the diffuseness was 1.37 fm instead of 1.30. Reasons for this are given below, but the results for the bound states in ^{19}F are essentially the same, and the binding energies and Coulomb displacements are just as well reproduced. The agreement for unbound states was less good, reflecting the approximations inherent in Buck and Pilt's treatment. The state of interest, with $2N + L = 9$, $L = 1$, appeared about 2 MeV lower than in Buck and Pilt's calculations, at $E_x = 13.1$ MeV with $\Gamma = 1.06$ MeV. It did not appear at all in the well with $V_0 = 116$ MeV, $a = 1.3$ fm as $\delta_{L=1}$ did not attain the value of $\frac{1}{2}\pi$.

When the Coulomb term was changed to that of ^{19}Ne , the $2N + L = 9$ states with $L = 1$ to 5, did not appear, for the same reason. However, the position of the $L = 1$ resonance could be expected to lie at $E_x \approx 13$ MeV also with a width of 4 MeV due to the increased height above threshold. This was rather larger than the

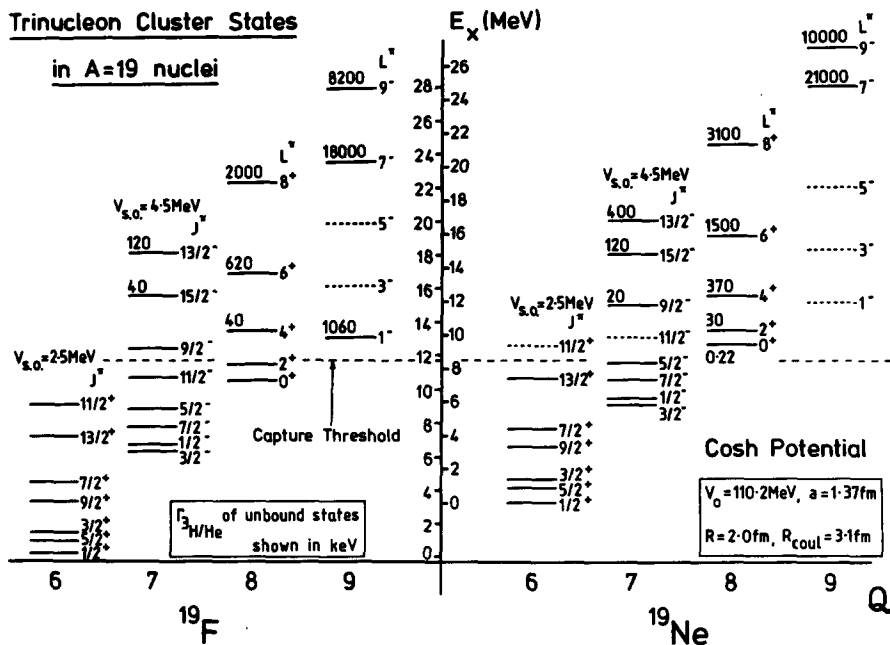


Fig. 18. Tri-nucleon cluster states in $A = 19$ nuclei. The states are labelled by J^π where the spin-orbit splitting is shown, and by L^π otherwise. The quantity Q is $2N+L$ for the light cluster. For unbound states, the ^3He or ^3H width is given in keV.

observed total width of 630 ± 130 keV, and if the resonance appeared at the experimental energy, then its width would rise to about 8 MeV. Since the ^3He width of a cluster state is related in a relatively unambiguous way to its excitation energy, it does not seem possible to identify the predicted states with $2N+L = 9$ with any state observed in the present experiments.

After the ^{19}F work, Buck and Pilt achieved success in accounting for the low-lying, negative-parity states of $A = 18$ nuclei in terms of $2N+L = 6$ tri-nucleon cluster states on a ^{15}N core¹⁵). These are the lowest states which can have all the cluster nucleons in the sd-shell and thus avoid problems of antisymmetrisation between these and the core nucleons, which in this model, only occupied the s- and p-shells. Calculations¹⁵) had shown that, in a cosh potential, the states within a band of fixed Q ($= 2N+L$) are split according to L in a rotational form, i.e.

$$E(Q) = C(Q) + AL(L+1).$$

In addition, the spin-dependent terms can be expressed in terms of three unknown strengths, for the spin-spin, tensor spin-spin and spin-orbit forces respectively. This gives an expression for the energy levels in terms of five free parameters, which were determined by Buck and Pilt by fitting low-lying experimental levels excited in tri-nucleon transfer.

In order to locate the higher states predicted by the cluster model, a cosh potential has been found which reproduces the values of $C(Q)$ and $A(Q)$ found by Buck and Pilt for the $Q = 6$ band. The radius was scaled according to $A_{\text{core}}^{1/3}$ from the ^{19}F well, and the depth and diffuseness were determined by fitting to be $V_0 = 107.9$ MeV, $a = 1.52$ fm. High-lying states in this well are shown in fig. 19.

The problem of extending the model to ^{17}F was that six oscillator quanta were needed to keep cluster and core nucleons in separate shells, and this is two more than the ground-state band. No tri-nucleon transfer data exist on states at this excitation, so well parameters were extrapolated from those for ^{19}F and ^{18}F . The calculated spectra for ^{19}F were fitted to the rotational expression used for ^{18}F , and a cosh potential well was determined which reproduced the resulting values of $C(Q)$ and $A(Q)$. The resulting well, with $V_0 = 110.2$ MeV, $a = 1.37$ fm differed slightly from the original well, but had the advantage, as mentioned above, in that it produced a $2N + L = 9$, $L = 1$ resonance. It was noted that the volume integral of the ^{18}F well was greater than both ^{19}F wells, not smaller, as might be expected. This discrepancy was also greater than the expected variation between neighbouring nuclei, and so V_0 and a for ^{17}F were taken to be the average of those for ^{18}F and ^{19}F , i.e. $V_0 = 109$ MeV, $a = 1.45$ fm. High-lying states in this well are shown in fig. 19.

The problem with the $^{17,18}\text{F}$ states is the same as that for ^{19}Ne . Those which may be observed in ^3He capture are generally lower than those seen in experiment,

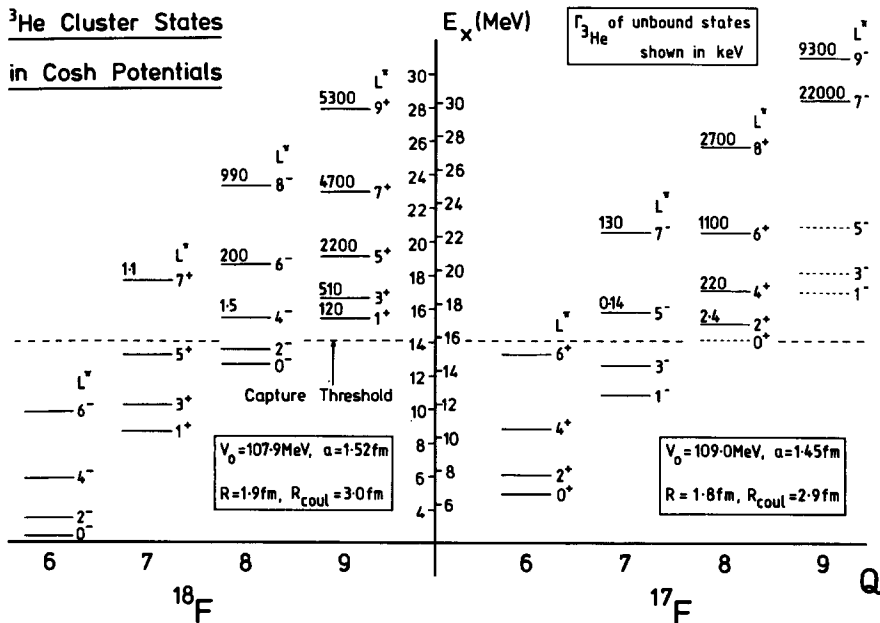


Fig. 19. Tri-nucleon cluster states in ^{17}F and ^{18}F . The notation is as in fig. 18.

and if the well parameters were adjusted to produce states at the experimental energies, the resulting states would be far too wide. Additionally, the radiative widths cannot readily be calculated, as the ground-state bands are not good cluster states, since both cluster and core nucleons share the $1p_{3/2}$ shell. Thus it seems that this simple cluster model cannot describe ^3He capture in this region. Apparently the cluster states are broken up in a way not accounted for in the model.

6. Analysis — the shell model

The principal difficulty in the application of the shell model to ^3He capture is the complexity of the capture states, since these are necessarily at a high excitation. Thus a considerable simplification of the model space must be used at all points in the calculation and therefore, detailed agreement cannot be expected. However, the validity of the weak-coupling approach has been demonstrated in many shell-model calculations²⁴), and one can hope for at least qualitative agreement using a truncated basis. In particular, quantities such as summed capture strengths may not be affected by the splitting of states not accounted for because of truncation of the model space. On the other hand, terms omitted from the basis can cause predicted strengths to fall below the values from a more complete calculation.

In the present work, simple wave functions (one configuration where possible) were used for the target nuclei and final states. Excited states of the compound nucleus were assumed to consist solely of configurations accessible by adding three nucleons to the target wave function and which could make an E1 transition to the final state. No other multipolarity was included, so the states were pure $1\hbar\omega$ excitations. No attempt was made to remove spurious states from the basis.

For all cases except ^{43}Ti , Kuo-Brown matrix elements were used²⁵). A full set for the s-, p-, sd- and pf-shells was used, and these did not include implicit p-shell excitations in the sd-values as they were included explicitly where needed. Single-particle energies for the sd- and pf-shells were based on resonances in a $^{15}\text{N}+p$ optical model potential with $V_0 = 78.5$ MeV, $a = 0.65$ fm, $r_0 = 1.1$ fm, $r_c = 1.25$ fm and a spin-orbit splitting of $1 \times L \cdot S$ MeV. During the course of the calculations it was found necessary to lower the energies for the 2p1f shell by 2 MeV, to obtain agreement with the capture data. The energies for the 1p and 2s1d shells were taken from experiment. The single-particle energies are shown in table 3. The procedure for ^{43}Ti will be discussed in subsect. 6.5. All calculations were carried out using the Oak Ridge-Rochester code MULTISHELL²⁶).

Where excited states predicted were few and widely separated, as in the cases of ^{17}F and ^{18}F , the strengths $(2J+1)\Gamma_{^3\text{He}}\Gamma_\gamma$ were estimated for each one. In other cases the density of states made individual $\Gamma_{^3\text{He}}$ calculations difficult and meaningless without a full *R*-matrix treatment, so $(2J+1)\Gamma_\gamma$ alone was calculated.

TABLE 3
Single-particle energies used in ${}^{17}\text{F}$, ${}^{18}\text{F}$, ${}^{19}\text{Ne}$ and ${}^{23}\text{Mg}$ calculations

Shell	$1p_{1/2}$	$1d_{5/2}$	$2s_{1/2}$	$1d_{3/2}$	$2p_{3/2}$	$2p_{1/2}$	$1f_{7/2}$	$1f_{5/2}$
$E_{s.p.}$ (MeV)	-14.8	0.0	0.1	5.0	7.0	10.0	13.1	20.1

The quantity $\Gamma_{3\text{He}}$ is given by the expression

$$\Gamma_{3\text{He}} = \frac{1}{2}\theta^2\Gamma_{s.p.},$$

where θ is the spectroscopic amplitude for the decomposition of the state into the target wave function and three nucleons in a relative s -state. $\Gamma_{s.p.}$ is the single-particle width and the factor of $\frac{1}{2}$ arises from isospin.

θ was calculated using methods outlined by Anyas-Weiss *et al.* ²⁷⁾ and Chew ²⁸⁾. $\Gamma_{s.p.}$ was estimated by taking the cosh potential used in the previous section and varying the depth to produce a resonance at the experimental energy. Its width was calculated as before from phase-shift behaviour. Fig. 20 shows a plot of $\Gamma_{s.p.}$ against resonant energy for $A = 19$ nuclei. These results are very similar to those obtained using a Saxon-Woods potential and the optical model parameters of

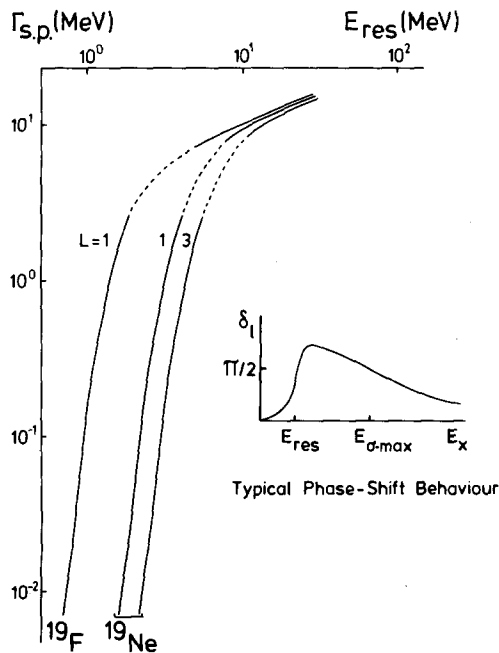


Fig. 20. Variation of the single-particle width with resonance energy for an unbound cluster state.

Cage *et al.*²⁹). There is also qualitative agreement with the method of Rolfs and Litherland³⁰) which involves the calculation of penetrabilities. The program used for calculating $\Gamma_{\text{s.p.}}$ was a version of the distorted wave code GREEN³¹) modified for a cosh potential.

6.1. CALCULATIONS FOR $^{16}\text{O}(^3\text{He}, \gamma)^{19}\text{Ne}$

The ground state of ^{16}O was assumed to be a closed $1p_{\frac{3}{2}}$ shell, and so the low-lying states of ^{19}Ne were considered as a pure $(\text{sd})^3$ configuration. As the $1d_{\frac{3}{2}}$ and $2s_{\frac{1}{2}}$ shells were so close together, but well separated from the $1d_{\frac{5}{2}}$ shell, the space was further restricted by omitting the $1d_{\frac{5}{2}}$ shell. Excited states were $(\text{sd})^2(\text{pf})$, the four pf-shells bringing the number of shells to six, which is the maximum allowed by MULTISHELL. ^{16}O single-particle energies were used, and low-lying $\frac{1}{2}^+$ and $\frac{5}{2}^+$ states and high-lying $\frac{1}{2}^-$, $\frac{3}{2}^-$, $\frac{5}{2}^-$, $\frac{7}{2}^-$ states (all $T = \frac{1}{2}$) were calculated.

This basis gave the two lowest states as:

$$\begin{aligned} |\frac{1}{2}^+\rangle &= 0.87(2s_{\frac{1}{2}})_{v=1}^3 - 0.41[(1d_{\frac{3}{2}})_{01}^2 2s_{\frac{1}{2}}] \\ &\quad + 0.21[(1d_{\frac{3}{2}})_{10}^2 2s_{\frac{1}{2}}] - 0.20(1d_{\frac{3}{2}})_{v=3}^3, \\ |\frac{5}{2}^+\rangle &= 0.59[1d_{\frac{3}{2}}(2s_{\frac{1}{2}})_{01}^2] - 0.47[(1d_{\frac{3}{2}}(2s_{\frac{1}{2}})_{10}^2] \\ &\quad - 0.42[(1d_{\frac{5}{2}})_{21}^2 2s_{\frac{1}{2}}] + 0.37(1d_{\frac{3}{2}})_{v=1}^3 \\ &\quad + 0.34[(1d_{\frac{3}{2}})_{30}^2 2s_{\frac{1}{2}}] - 0.02(1d_{\frac{3}{2}})_{v=3}^3, \end{aligned}$$

where v is the seniority. It was not possible to calculate γ_2 transitions to the $\frac{1}{2}^-$ state at 275 keV. This is a non-normal parity state and thus beyond the scope of the model, although experimentally γ_1 and γ_2 could not be separated.

The model does not predict one state with large E1 strength, with weaker states giving rise to fine structure, but rather, the γ_{0+1} strength is split amongst a large number of states, centred around an excitation energy of 18 MeV. It was not practicable to calculate $\Gamma_{^3\text{He}}$ for each one, together with their relative phases, so the quantity $(2J+1)\Gamma_\gamma$ was calculated, and was summed in bins of 500 keV excitation and plotted as a histogram (fig. 21). The shape of the experimental excitation function should show a qualitative resemblance to this histogram after allowance for (i) the variation of ^3He width from state to state, and (ii) the broadening of peaks in the histogram resulting from the finite total widths of the individual states. The quantity $(2J+1)\Gamma_\gamma$ appears in the sum rule due to Levinger³²),

$$\sum_J (2J+1)\Gamma_\gamma = 4(2J_f+1) \frac{e^2}{\hbar c} \frac{NZ}{A} \frac{E_\gamma^2}{mc^2}.$$

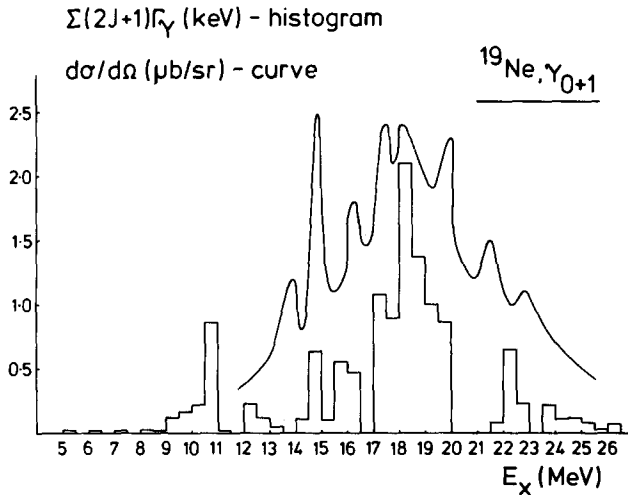


Fig. 21. The histogram shows the distribution of $(2J+1)\Gamma_\gamma$ from shell-model states calculated for ^{19}Ne . The curve is the experimental excitation function.

The shape of the γ_{0+1} excitation function is well reproduced by the shell-model calculations. Most of the strength lies between $E_x = 17$ and 20 MeV and the smaller experimental peaks at 14.88 , 16.24 and ≈ 22 MeV also appear. The calculated peak just below 11 MeV would have a very small $\Gamma_{^3\text{He}}$ due to the Coulomb barrier, and is therefore not seen. A total $(2J+1)\Gamma_\gamma$ of 11.3 keV is seen in the excitation region between 12 and 26 MeV on the calculated histogram. An experimental lower limit on this quantity can be derived by summing the contributions to $(2J+1)\Gamma_{^3\text{He}}\Gamma_\gamma$ for individual resonances, and using the limit

$$\Gamma \geq \Gamma_{^3\text{He}}.$$

This method gives an experimental value of

$$\sum (2J+1)\Gamma_\gamma \geq 3.9 \text{ keV},$$

which is consistent with the calculated value. The total strength to all calculated states is 13.5 keV, which is again consistent with the total experimental yield which gives

$$\sum (2J+1)\Gamma_\gamma \geq 4.1 \text{ keV}.$$

The position and width of the experimental yield has the appearance of a GDR. However, on the assumption that the yield is dominantly to the $J^\pi = \frac{5}{2}^+$ first

excited state, the Levinger sum rule quoted above predicts

$$\sum (2J+1)\Gamma_\gamma = 286 \text{ keV}$$

for $E_\gamma = 18 \text{ MeV}$. Thus, if the GDR is involved in this reaction, it is excited only weakly presumably because of the small number of configurations that are accessible to ^3He capture. Configurations of the form $(1p_{\frac{1}{2}})^{-1}(2s1d)^4$ can also make γ_0/γ_1 transitions but have been excluded by this model, as have all $T = \frac{3}{2}$ states.

6.2. CALCULATIONS FOR $^{15}\text{N}(^3\text{He}, \gamma)^{18}\text{F}$

In this case, the γ_0 yield is to the 1^+ , $T=0$ ground state, and γ_{1-4} to the unresolved 0^- , 3^+ and 5^+ $T=0$ states and a 0^+ , $T=1$ state. States decaying to the ground state were assumed to be either 0^- , 1^- or 2^- , $T=1$ states.

The ground-state wave function of ^{15}N has been calculated by Zuker³³) to be

$$0.88(1p_{\frac{1}{2}})^{-1} + 0.44(1p_{\frac{1}{2}})^{-3}(1d_{\frac{3}{2}})_{01}^2 + \dots$$

For the purposes of the present calculation a pure $1p_{\frac{1}{2}}$ hole was assumed, and so excited states of ^{18}F were either $1p_{\frac{1}{2}}^{-1}(\text{sd})^3$ or $(\text{sd})(\text{pf})$. The ^{18}F ground state, when restricted to two nucleons in the $1d_{\frac{3}{2}}$ or $2s_{\frac{1}{2}}$ shells, was found to be:

$$|1^+, 0\rangle = 0.10(1d_{\frac{3}{2}})^2 + 0.99(2s_{\frac{1}{2}})^2.$$

For the state to be almost pure $(2s_{\frac{1}{2}})^2$ was surprising, so, as a check, the basis was increased to include $1d_{\frac{3}{2}}$, and then the Elliott and Flowers result³⁴) was well reproduced. MULTISHELL with Kuo-Brown matrix elements gave

$$0.43(1d_{\frac{3}{2}}^2) - 0.52(1d_{\frac{3}{2}}1d_{\frac{3}{2}}) - 0.04(1d_{\frac{3}{2}}^2) - 0.09(2s_{\frac{1}{2}}1d_{\frac{3}{2}}) + 0.73(2s_{\frac{1}{2}}^2),$$

while Elliott and Flowers found (with the ordering and phase conventions made compatible)

$$0.58(1d_{\frac{3}{2}}^2) - 0.57(1d_{\frac{3}{2}}1d_{\frac{3}{2}}) - 0.19(1d_{\frac{3}{2}}^2) - 0.02(2s_{\frac{1}{2}}1d_{\frac{3}{2}}) + 0.55(2s_{\frac{1}{2}}^2).$$

For the sake of simplicity the ground state was therefore assumed to be pure $(2s_{\frac{1}{2}})^2$, and the omission of the $1d_{\frac{3}{2}}$ shell greatly simplified the basis. A particle in the $1f_{\frac{7}{2}}$ or $1f_{\frac{5}{2}}$ shell could not make an E1 transition to the $2s_{\frac{1}{2}}$ shell and so the only active shells were $1p_{\frac{1}{2}}$, $2s_{\frac{1}{2}}$, $1d_{\frac{3}{2}}$, $2p_{\frac{1}{2}}$ and $2p_{\frac{3}{2}}$, i.e. within the scope of MULTISHELL.

Unlike the ^{19}Ne model, this 5-shell calculation restricted to a one-configuration ground state produced only a small number of strongly excited states. It was

TABLE 4
Shell-model states of ^{18}F with capture strength $> 1 \text{ keV}^2$

Decay	J^π, T	E_γ (MeV)	$\Gamma_{\text{s.p.}}$ (MeV)	$\Gamma_{^3\text{He}}$ (keV)	Γ_γ (eV)	$(2J+1)\Gamma_{^3\text{He}}\Gamma_\gamma$ (keV 2)
γ_0	$0^-, 1$	23.82	9.4	5.3	4384	23
		19.30	7.2	52.1	32.8	5.1
		20.71	8.0	13.8	22.8	1.0
		22.73	9.0	280	591	496
		23.89	9.5	0.43	3547	4.6
	$2^-, 1$	19.93	7.5	379	9.1	17
		20.99	8.1	159	5.7	4.5
		21.90	8.6	37.4	154	29
		23.60	9.4	113	3283	1850

possible to calculate the individual ^3He widths, and those with capture strengths $> 1 \text{ keV}^2$ are given in table 4.

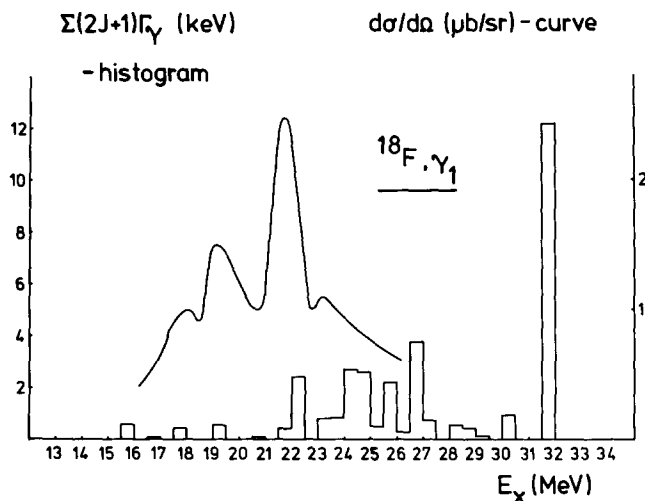
The 1^- state in the γ_0 yield predicted to lie at 22.7 MeV (table 4) is a good candidate for the peak seen at this energy with a similar strength (table 1). If this is the case, the very strong 2^- state predicted at 23.6 MeV probably corresponds to the peak seen at 20.1 MeV, although the strengths agree only qualitatively. On the other hand, both experimental peaks are observed in γ_{1-4} also, and so, making the usual assumptions of multipolarity, these must be $2^- \rightarrow 3^+$ (i.e. γ_1) transitions. It is possible that both peaks seen in γ_0 are 2^- resonances and the shell-model strength is split between them; this is 1850 keV^2 compared with a total observed of $1810 \pm 250 \text{ keV}^2$. If this were so, the 0^- and 1^- strengths may form some hidden, underlying structure.

Table 4 shows that for each J_i^π , the major proportion of the total radiative width is due to the highest state. A total $(2J+1)\Gamma_\gamma$ of 34 keV is calculated (the sum rule for $E_\gamma = 20 \text{ MeV}$ is 112 keV) of which 48 % is the highest 2^- state. The relatively large fraction (32 %) of the sum rule limit observed here is consistent with the excitation of the GDR in this case.

Making this assumption, a second calculation was made to account for the structure seen in γ_{1-4} in terms of the $2^- \rightarrow 3^+$ transition. Reproduction of the 3^+ state in shell-model terms required the $1d_{3/2}$ shell. Following the example of Elliott and Flowers³⁴⁾ and restricting the space to a maximum of one $1d_{3/2}$ nucleon, the wave function was found to be

$$|3^+\rangle = 0.20(1d_{3/2}1d_{3/2}) - 0.87(1d_{3/2}2s_{1/2}) - 0.44(1d_{3/2}^2).$$

Building $1\hbar\omega$ excitations on this state required the $2p1f$ shells, but as only 6 shells were permitted the $1f$ shells were omitted. The basis for the excited states was

Fig. 22. As fig. 21, for ^{18}F .

therefore very similar to that used in the γ_0 calculation, giving the two cases some degree of consistency, even if some capture strength was left unaccounted for.

The calculated strength, like that for ^{19}Ne , was split between many states, and the histogram of $(2J+1)\Gamma_\gamma$ is shown in fig. 22. The general shape of the calculated yield is reasonably consistent with that of the experimental excitation function, but the calculated excitation energy is again too high, this time by about 4 MeV.

6.3. CALCULATIONS FOR $^{14}\text{N}(^3\text{He}, \gamma)^{17}\text{F}$

The lowest two states of ^{17}F were considered to be simple one-particle configurations: $1d_{3/2}$ for the $\frac{5}{2}^+$ ground state, and $2s_{3/2}$ for the $\frac{1}{2}^+$ first excited state. The ^{14}N ground state was taken as $(1p_{3/2}^{-2})_{1,0}$.

For the γ_1 yield, the complete basis of configurations accessible by $(^3\text{He}, \gamma(E1))$ comprised only five shells as neither the $1d_{3/2}$ nor the $1f$ shells were needed. States with capture strength $\geq 1 \text{ keV}^2$ are shown in table 5. A possible correspondence between theory and experiment exists in that the peak observed at 21.3 MeV may be the $63 \text{ keV}^2 \frac{3}{2}^-$ strength predicted to lie at 21.85 MeV. However, the $\frac{1}{2}^-$ state calculated to have a strength of 336 keV^2 at 21.38 MeV is more problematic; the entire γ_1 yield observed has a strength of only $140 \pm 30 \text{ keV}^2$. Although this model is very similar to that used for $^{18}\text{F} \gamma_0$, the results are much worse. The overall position of the yield is well reproduced, but the total strength is overestimated by a factor of 3.

In order to make a qualitative prediction of the γ_0 yield, the basis was extended to $1p_{3/2}$, $1d_{3/2}$, $1d_{5/2}$, $2p_{3/2}$, $1f_{7/2}$ and $1f_{5/2}$. This was not complete; the $2p_{3/2}$ shell had to be omitted to keep the number down to six. The results, shown in table 5, again

TABLE 5
Shell-model states of ^{17}F with capture strength $> 1 \text{ keV}^2$

Decay	J^π, T	E_γ (MeV)	$\Gamma_{s.p.}$ (MeV)	$\Gamma_{^3\text{He}}$ (keV)	Γ_γ (eV)	$(2J+1)\Gamma_{^3\text{He}}\Gamma_\gamma$ (keV 2)
γ_0	$\frac{3}{2}^-, \frac{1}{2}$	20.57	7.0	27.9	485	54
		21.79	7.7	14.1	96	5.4
	$\frac{5}{2}^-, \frac{1}{2}$	19.02	5.5	8.5	119	6.0
		22.67	8.1	0.4	401	1.0
		25.58	9.5	6.4	768	29.4
	$\frac{7}{2}^-, \frac{1}{2}$	19.94	6.5	30.7	7	1.6
		20.68	7.0	1395	427	4770
		21.95	7.7	369	202	595
		29.18	10.5	336	4264	11460
	$\frac{1}{2}^-, \frac{1}{2}$	21.38	7.4	143	1174	336
		20.17	6.6	13.7	17	1.0
	$\frac{3}{2}^-, \frac{1}{2}$	21.85	7.7	17.6	894	63

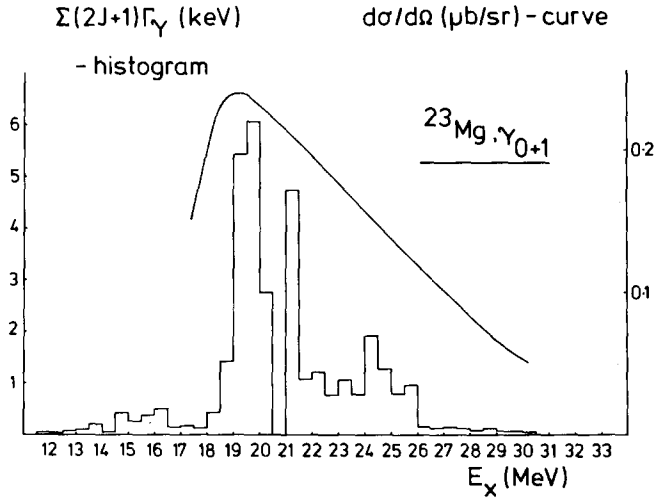
overestimate the observed strengths. The strongest state at 29.2 MeV is almost pure $(1p_{\frac{1}{2}})^4 1f_{\frac{3}{2}}$ and would therefore have too high a proton width ($\geq 10 \text{ MeV}$) to be observed. However, the $\frac{7}{2}^-$ state at 20.68 MeV, although well placed, is fifteen times stronger than the total observed γ_0 yield. It is difficult to see how even the least accurate part of the calculation, that of $\Gamma_{^3\text{He}}$, could give rise to such a discrepancy.

The shell-model calculations of Harakeh *et al.*³⁵⁾ use a larger basis than in the present work, and their radiative widths and positions agree well with their own $^{16}\text{O}(p, \gamma_{0+1})^{17}\text{F}$ experiment and the present $^{14}\text{N}(^3\text{He}, \gamma_{0+1})^{17}\text{F}$ results. They concluded that the GDR was being excited in the $^{16}\text{O}(p, \gamma)^{17}\text{F}$ reaction, and since the excitation functions of the two reactions are similar it is possible that ^3He capture also excites the GDR.

6.4. CALCULATIONS FOR $^{20}\text{Ne}(^3\text{He}, \gamma)^{23}\text{Mg}$

The low-lying $\frac{3}{2}^+$ and $\frac{5}{2}^+$ states of ^{23}Mg were assumed to be (sd)⁷ and the excited states (sd)⁶(pf). The lower states had to be further restricted to $(1d_{\frac{3}{2}})^6(2s_{\frac{1}{2}})$ or $(1d_{\frac{3}{2}})^7$, because of limitations in the program MULTISHELL. This arbitrary restriction implied that the calculations could only be schematic. In spite of this, the separation of the two lowest states was well reproduced: 440 keV as opposed to the experimental value of 450 keV.

As with ^{19}Ne , the γ_{0+1} strength is split between a large number of states. The histogram of $(2J+1)\Gamma_\gamma$ is shown in fig. 23, and again, the shape of the excitation

Fig. 23. As fig. 21, for ^{23}Mg .

function is well reproduced. Most of the strength is shown to lie between 19 and 20 MeV, and the remaining strength is all above this, giving rise to the skew experimental peak. There is slight evidence for structure in the observed yield between 24 and 25 MeV and a small peak occurs in the histogram at this energy.

A total $(2J+1)\Gamma_\gamma$ of 35 keV is calculated for γ_{0+1} out of a sum rule limit of 645 keV ($E_\gamma = 19$ MeV). Thus, although the energy and shape of this excitation function are consistent with those of a giant resonance, it appears that again the small number of states accessible to ^3He capture results in a weak excitation of the GDR.

6.5. CALCULATIONS FOR $^{40}\text{Ca}(^3\text{He}, \gamma)^{43}\text{Ti}$

The ^{40}Ca ground state was considered to be a fully closed $1d_{3/2}$ shell and the low-lying states of ^{43}Ti to be pure $(1f_{7/2})^3$. The excited states were thus $(1f_{7/2})^2(\text{sdg})$, but the E1 condition reduced the number of active shells to four: $1f_{7/2}$, $1g_{7/2}$, $2d_{3/2}$ and $1g_{9/2}$. Because of limitations in MULTISHELL, the $1g_{9/2}$ shell had to be excluded from the calculations.

Single-particle energies were estimated from two considerations. Firstly, one oscillator quantum was typically $41A^{-1/3}$ MeV, or 11.7 MeV for $A = 43$, and this gave the gap between the centroids of the pf- and sdg-shells. Secondly, the spin-orbit splitting was taken as $(2L+1) \times 1$ MeV, which was 9 MeV for the $1g$ shells. Hence the energies of the $2d_{3/2}$, $1g_{7/2}$ and $1g_{9/2}$ shells with respect to the $1f_{7/2}$ were estimated to be 12, 14 and 5 MeV respectively. Because the $1g_{9/2}$ shell lies so low in energy, it is unlikely that its exclusion from the calculation makes a large difference to the predicted E1 strengths.

The four parameters required to calculate the MSDI matrix elements³⁶⁾ were not well established for the sdg-shell, so they were estimated by extrapolation from better-known 2p1f values. The reliability of this procedure is doubtful but was the only one available without actually fitting the parameters to experimental levels. Making the reasonable assumption that the lowest $\frac{3}{2}^-$ and $\frac{7}{2}^-$ states are pure $(1f_{7/2})^3$, the model calculates the $\frac{7}{2}^-$ to be 1.92 MeV below the $\frac{3}{2}^-$ instead of 0.48 MeV above. Thus the matrix elements are probably not reliable.

The histogram of the radiative widths of the high-lying states (fig. 24) does however show structure similar to that seen in experiment. Most of the strength is clustered into a fairly symmetrical single peak centred at 18 MeV above the $\frac{3}{2}^-$ state. The total calculated $(2J+1)\Gamma_\gamma$ was very small, 1 keV, but this is probably due to an incomplete basis and unrealistic matrix elements.

Experimentally, the general shape of the excitation function is again characteristic of that of a GDR, but the small cross sections observed, as in other excitation functions presented here, imply that if the GDR is responsible, it is excited only weakly.

7. Conclusions

The preceding two sections have shown that the shell model gives, in general, a better description of the data than does the cluster model. The main restriction of this cluster model is that two states 20 MeV apart have to be good cluster states and describable using the same cluster-core interaction for each. Even where this is possible, for capture onto doubly magic nuclei, the correspondence between obser-

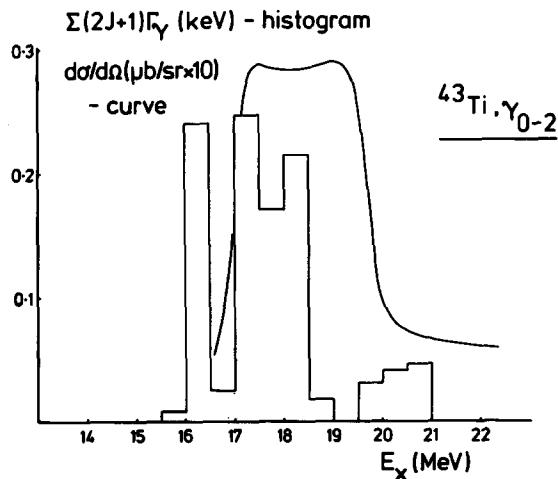


Fig. 24. As fig. 21, for ^{43}Ti .

ved resonances is at best only qualitative. On the other hand, the shell model has as broad a basis as required and does not depend on one potential well for the description of widely separated states.

For the present calculations, the shell model has been used with truncated bases, but in spite of this, the results have only been seriously at variance with experiment in the case of ^{17}F . Broad structure has been well reproduced in general. Often the results are consistent with the excitation of the GDR in these ^3He capture experiments, but the excitation is always much weaker than in proton capture. The shell-model calculations suggest that this is a result of the smaller number of configurations, present in the GDR, that can be reached by ^3He capture. Fine structure, too, has been within the scope of the model, and has been most accurately reproduced in the ^{19}Ne calculations. There seems to be no reason why the use of sufficiently large shell-model bases, together with better established single-particle energies, should not be capable of explaining the more detailed features of the ^3He capture.

An important result of the calculations has been the placing of the $2p_{1/2}$ shell single-particle energies, which were not well established in this region. Values of 7, 10, 13.1 and 20.1 MeV with respect to $1d_{3/2}$, for the $2p_{3/2}$, $2p_{1/2}$, $1f_{7/2}$ and $1f_{5/2}$ shells respectively, have been found to reproduce the ^{19}Ne and ^{23}Mg data very well.

The authors would like to thank Professor K. W. Allen for the use of the facilities at the Oxford Nuclear Physics Laboratory, and the Science Research Council for the provision of a research grant. One of us (C.E.W.) would like to thank the SRC for a student grant.

References

- 1) J. L. Black, W. J. Caelli, W. F. Davidson and R. B. Watson, Nucl. Phys. **A153** (1970) 233
- 2) S. L. Blatt, A. M. Young, S. C. Ling, K. J. Moon and C. D. Porterfield, Phys. Rev. **176** (1969) 1147
- 3) F. Nüsslin, H. Werner and J. Zimmerer, Z. Naturf. **21** (1966) 1195
- 4) A. M. Young, S. L. Blatt and R. G. Segler, Phys. Rev. Lett. **25** (1970) 1764
- 5) E. Ventura, C. C. Chang and W. E. Meyerhof, Nucl. Phys. **A173** (1971) 1
- 6) W. Del Bianco, J. C. Kim and G. Kajrys, Can. J. Phys. **56** (1978) 1054
- 7) N. G. Puttaswamy and D. Kohler, Phys. Lett. **20** (1966) 288
- 8) H. D. Shay, R. E. Peschel, J. M. Long and D. A. Bromley, Phys. Rev. **C9** (1974) 74
- 9) E. Ventura, E. M. Diener, C. C. Chang, S. S. Hanna and G. A. Fischer, Bull. Am. Phys. Soc. **17** (1972) 113
- 10) S. H. Chew, J. Lowe, J. M. Nelson and A. R. Barnett, Nucl. Phys. **A229** (1974) 241
- 11) S. H. Chew, J. Lowe, J. M. Nelson and A. R. Barnett, Nucl. Phys. **A283** (1977) 445
- 12) T. Mo, R. A. Blue and H. R. Weller, Nucl. Phys. **A197** (1972) 290
- 13) W. F. Davidson, J. L. Black, M. R. Najam and B. M. Spicer, Nucl. Phys. **A168** (1971) 399
- 14) B. Buck and A. A. Pilt, Nucl. Phys. **A280** (1977) 133
- 15) B. Buck and A. A. Pilt, Nucl. Phys. **A295** (1978) 1
- 16) A. A. Pilt, private communication
- 17) S. H. Chew, J. Lowe, J. M. Nelson and A. R. Barnett, Nucl. Phys. **A286** (1977) 451

- 18) J. Lowe and G. J. Lowe, Birmingham University Nuclear Structure Group Report, (1977) p. 122, unpublished
- 19) F. Ajzenberg-Selove, Nucl. Phys. **A300** (1978) 1
- 20) F. Ajzenberg-Selove, Nucl. Phys. **A281** (1977) 1
- 21) P. M. Endt and C. van der Leun, Nucl. Phys. **A310** (1979) 1
- 22) F. Ajzenberg-Selove and T. Lauritsen, Nucl. Phys. **A227** (1974) 1
- 23) I. Linck, L. Kraus and S. L. Blatt, Phys. Rev. **C21** (1980) 791
- 24) A. P. Zuker, Proc. Int. Conf. on nuclear structure and spectroscopy, Amsterdam, 1974, ed. H. P. Blok and A. E. L. Dieperink (North-Holland, Amsterdam, 1974), p. 115
- 25) T. T. S. Kuo and G. E. Brown, Nucl. Phys. **85** (1966) 40
- 26) J. B. French, E. C. Halbert, J. B. McGrory and S. S. M. Wong, Adv. in Nucl. Phys. **3** (1969) 193
- 27) N. Anyas-Weiss, J. C. Cornell, P. S. Fisher, P. N. Hudson, A. Menchaca-Rocha, D. J. Millener, A. D. Panagiotou, D. K. Scott, D. Strottman, D. M. Brink, B. Buck, P. J. Ellis and T. Engeland, Phys. Reports **12C** (1974) 201
- 28) S. H. Chew, Ph. D. thesis, University of Birmingham (1976), unpublished
- 29) M. E. Cage, D. L. Clough, A. J. Cole, J. B. A. England, G. J. Pyle, P. M. Rolph, L. H. Watson and D. H. Worledge, Nucl. Phys. **A183** (1972) 449
- 30) C. Rolfs and A. E. Litherland, Nuclear spectroscopy and reactions, part C, ed. J. Cerny (Academic Press, 1974) p. 162
- 31) W. D. Hay and S. M. Perez, Two subroutines for the calculation of distorted waves, Oxford University Nuclear Physics Theoretical Group Report No. 42, 1969
- 32) J. S. Levinger, Nuclear photo-disintegration (Oxford University Press, London, 1960)
- 33) A. P. Zuker, B. Buck and J. B. McGrory, Phys. Rev. Lett. **21** (1968) 39
- 34) J. P. Elliott and B. H. Flowers, Proc. Roy. Soc. **229** (1955) 536
- 35) M. N. Harakeh, P. Paul and P. Gorodetzky, Phys. Rev. **C11** (1975) 1008
- 36) P. W. M. Glaudemans, P. J. Brussaard and B. H. Wildenthal, Nucl. Phys. **A102** (1967) 593;
P. J. Brussaard and P. W. M. Glaudemans, Shell model applications in nuclear spectroscopy (North-Holland, Amsterdam, 1977)